INSTITUT DE FRANCE
Académie des sciences

# Comptes Rendus
# Physique

Nasim Mohammadi Estakhri and Nader Engheta

**Tunable metasurface-based waveplates - A proposal using inverse design**

Volume 21, issue 7-8 (2020), p. 625-639

Published online: 3 November 2020
Issue date: 19 January 2021

https://doi.org/10.5802/crphys.5

**Part of Special Issue:** Metamaterials 2
**Guest editors:** Boris Gralak (CNRS, Institut Fresnel, Marseille, France) and Sébastien Guenneau (UMI2004 Abraham de Moivre, CNRS-Imperial College, London, UK)



*Les* Comptes Rendus. Physique *sont membres du Centre Mersenne pour l'édition scientifique ouverte*
www.centre-mersenne.org
e-ISSN : 1878-1535

*Comptes Rendus*
*Physique*
**2020**, 21, nº 7-8, p. 625-639
https://doi.org/10.5802/crphys.5

Metamaterials 2 / *Métamatériaux 2*

# Tunable metasurface-based waveplates - A proposal using inverse design

## *Lames à retard d'onde accordables à base de métasurfaces - Une approche par conception inverse*

**Nasim Mohammadi Estakhri**[a] **and Nader Engheta**[*, a]

[a] Department of Electrical and Systems Engineering, University of Pennsylvania, Philadelphia, PA 19104, USA

*E-mails:* esmo@seas.upenn.edu (N. Mohammadi Estakhri), engheta@seas.upenn.edu (N. Engheta)

**Abstract.** An approach to achieve tunable free-space waveplate operation based on a two-layer cascaded metastructure is proposed. Phase retardation is varied through changing the axial distance between the two layers. Full control on the ellipticity of the output wave is attained with wavelength-scale variations in the axial distance. The theoretically desired characteristics of the metastructures are presented and multiple physical implementations are suggested based on inverse design topology optimization.

**Résumé.** Une approche est proposée pour obtenir un retard de phase d'onde électromagnétique accordable en s'appuyant sur une méta-structure avec deux couches planes en regard l'une de l'autre. Le retard de phase est ajusté par l'intermédiaire de la variation de la distance axiale entre les deux couches. Un contrôle complet de l'ellipticité de l'onde en sortie de dispositif est atteint avec des variations de la distance axiale à l'échelle de la longueur d'onde. Les caractéristiques désirées des méta-structures sont présentées et plusieurs applications physiques sont suggérées, en s'appuyant sur des optimisations topologiques ou des algorithmes génétiques par conception inverse.

**Keywords.** Polarization, Waveplates, Tunability, Topology optimization, Inverse design, Metastructures.

**Mots-clés.** Polarisation, Lames d'onde, Accordabilité, Optimisation topologique, Conception inverse, Méta-matériau.

Available online 16th October 2020

* Corresponding author.

## 1. Introduction

Generation of controllable ellipticity and tunable polarized light in a single device could enable a variety of applications in optical devices and set-ups, such as polarization cameras and material characterization. Waveplates are conventionally built using natural birefringent crystals which provide different effective indices depending on the polarization and direction of the incident wave. While propagating inside the crystal, a phase shift (retardation) is gradually created between two orthogonally polarized waves aligned with fast- and slow-axes of the crystal. Due to the small birefringence (e.g. $\Delta n \simeq 9 \times 10^{-3}$ for quartz crystal at 633 nm [1]), such devices are typically multiple-wavelengths thick and less desirable for direct integration purposes. Alternatively, an approach that may provide potentially thinner solutions which are more suitable for integration purposes is to use metastructures (a general term we use hereafter referring to metasurfaces and metamaterials). Orientation, dimensions, material properties, and geometrical shape of surface elements in metastructures have been optimized to create the desired retardation between orthogonal polarizations, e.g. to create electromagnetically thin quarter-wave plates and halfwave plates [2–13], both in transmission and reflection modes. In addition to the smaller size, designer metastructures provide a platform to enforce application-based characteristics as the response is not anymore limited by the naturally available birefringent materials. For instance, attaining specific bandwidth of operation, angular dispersion, loss, etc. may be targeted using metastructure-based waveplates. In this article we propose a new scheme to attain phase shift "tunability" in a planar waveplate consisting of two cascaded metastructures and with close to ideal conversion efficiencies. One of the main advantages of our proposed platform resides in the fact that the controllable retardation is independent from the specifics of the employed metastructures. We show that by using a pair of metastructures as polarization-dependent beam splitters (anisotropic anomalous refraction), it is possible to achieve any amount of retardation simply through adjusting the distance between the two cascaded metastructures. Polarization sensitive anomalous refraction is implemented using the inverse topology optimization technique. These techniques have gained increasing amount of interest in the recent years due to relatively fast convergence and versatile range of applications [14–23]. The tunability can be expressed as a linear dependence between the retardation and the physical distance between the layers. Fast- and slow-axes of the structure are also automatically specified in the design and there is no need for additional steps to determine them, as required in conventional birefringent crystals. Previously reported tunable waveplates have relied on several reconfigurable elements to achieve some range of phase tunability, including incorporation of liquid crystals [24–26], phase change materials [27, 28], and electromechanically actuated capacitor arrays [29]. Our proposed waveplates, by contrast, are formed by two metasurfaces whose axial separation is the only movable part. In the following we will present the theoretical formulation of the transfer function of the waveplate in Section 2, followed by two sets of numerical examples in Sections 3 and 4. We will also look into several cases including oblique incidence and extreme refraction.

## 2. Theoretical formulation

### 2.1. *Idea and formulation: normal incidence*

Figure 1 illustrates the idea of the tunable free-space wave-plate configuration. Two planar metastructures (depicted with roman numbers I and II) are placed parallel to each other and with a finite distance "$d$" along the $x$-axis. Each metastructure has a thickness of "$h$" in the $x$-direction and it is periodic in the $y$-direction with fundamental periodicity of "L" (one period is shown in Figure 1). While the metastructures may be designed in the most general format, a two-dimensional (2D) configuration which is $z$-invariant in our arrangement is in principle sufficient

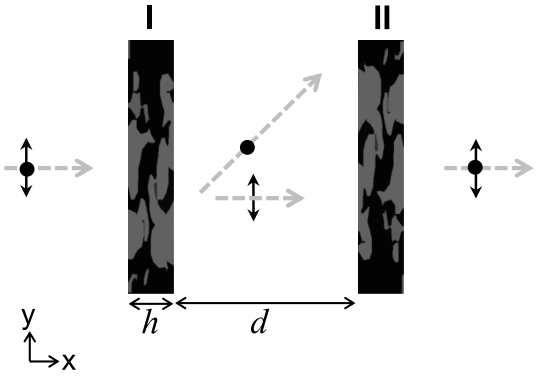


**Figure 1.** Polarization-dependent phase control. Schematic illustration of the idea of tunable waveplate metastructures. Two planar 2D (i.e. $z$-invariant) metastructures (I and II) are placed parallel to each other, each with thickness of "$h$" in the direction of wave illumination and period of "L" in $y$-direction. The two metastructures are identical in all aspects, except their placement orientation. Metastructure II is the mirror image of metastructure I in both $x$- and $y$-directions, i.e., it is rotated 180° around the $z$ axis. In the example shown, metastructures only affect the momentum of TE waves (i.e. electric field polarized out-of-plane), but not the momentum of TM waves. Due to their arrangement, the change in the momentum imposed by the first structure is canceled out by the second one, creating a controllable phase retardation between the two polarizations.

to achieve polarization control and therefore it is not necessary to assume a 3D patterning. The distribution of the permittivity inside each metastructure is optimized according to the goal functions discussed in the following.

Waveplates (also known as wave retarders) operate based on creating a phase shift between two orthogonal polarizations whose orientations are specified based on the optical axis of the waveplate [30]. Although using metasurfaces have enabled a large variety of ultrathin polarizing elements, extensive parametric studies are typically required to attain the required phase shift (retardation) between the orthogonal polarization [5–13]. Quite contrary, here we rely on the difference in the imposed momentum on the Transverse Electric (TE) and Transverse Magnetic (TM) incident waves to attain controllable phase retardation [31]. As a result, once the core metastructure (as in Figure 1, metastructure I) is designed, the system can be tuned to create any desired phase shift between the two orthogonal incident waves. In other words, the retardation is determined by the arrangement (e.g. distance) of the two metastructures rather than intrinsic properties of each surface.

Assuming a monochromatic plane wave normally incident on the structure from left to right in Figure 1, the role of metastructure I is set to impose an abrupt, polarization-sensitive momentum change on the impinging wave. Upon refraction through the metastructure I, the TE incident wave is tilted by an angle of $\theta_{\mathrm{TE}}$ which, as an example, is set at 45° throughout this article, and the TM incident wave is tilted by an angle of $\theta_{\mathrm{TM}} \neq \theta_{\mathrm{TE}}$ which we set at 0° hereafter. Metastructure I therefore operates similar to a polarization beam splitter, yet implemented with a planar and potentially thin structure. As the wave propagates beyond metastructure I, assuming $e^{j\omega t}$ time-harmonic convention, the total electric field may be written as,

$$\begin{aligned}\mathbf{E}_{\mathrm{total},1} = {} & \cos\theta_{\mathrm{TM}}{}^{-1/2}(\mathbf{y}\cdot\mathbf{E}_i)[\mathbf{y}\cos\theta_{\mathrm{TM}} - \mathbf{x}\sin\theta_{\mathrm{TM}}]e^{-jk_0(x\cos\theta_{\mathrm{TM}}+y\sin\theta_{\mathrm{TM}})+j\varphi_{\mathrm{TM},1}} \\ & + \cos\theta_{\mathrm{TE}}{}^{-1/2}(\mathbf{z}\cdot\mathbf{E}_i)\mathbf{z}e^{-jk_0(x\cos\theta_{\mathrm{TE}}+y\sin\theta_{\mathrm{TE}})+j\varphi_{\mathrm{TE},1}} \end{aligned} \quad (1)$$

indicating the polarization dependent beam splitting effect. Notably, the cumulative propagation phases of the two polarizations are different and depends on the refraction angles $\theta_{\mathrm{TM}}$ and $\theta_{\mathrm{TE}}$. Note that in writing (1) we assume an ideal transmission response, meaning that reflected waves from metastructure I (for both co- and cross-polarizations) are negligible. Here, $\mathbf{E}_i$ is the incident electric field vector lying in the $y$–$z$-plane, $k_0$ is the free space wave number, and $\varphi_{\mathrm{TM},1}$ and $\varphi_{\mathrm{TE},1}$ are constant phases added to TM and TE waves upon traversing metastructure I. While the phase difference between the two polarizations varies upon propagation, the two waves are also angularly separated after metasurface I. In order to restore the original wavefront of the incident wave we use a second metastructure (as shown in Figure 1 with metastructure II), whose role is to restore the original momentum of both polarizations. This means that the TE and TM waves must be rotated by angles of $-\theta_{\mathrm{TE}}$ and $-\theta_{\mathrm{TM}}$, respectively. Interestingly, in order to restore the original momentum of the incident wave components it is not required to separately design a second metastructure from scratch. Indeed, investigating Figure 1, the trajectory of waves traversing metastructure II are identical to the trajectory of their interaction with metastructure I when they are time-reversed. As a result, it is sufficient to use an identical design for both metastructures, while the second structure is rotated 180° around the $z$-axis compared to the first one. Again, assuming ideal transmission with zero reflection by metastructure II, the total outgoing electric field beyond metastructure II then takes the following form,

$$\mathbf{E}_{\mathrm{total},2} = e^{-jk_0x}[(\mathbf{y}\cdot\mathbf{E}_i)\mathbf{y}e^{-jk_0d\cos\theta_{\mathrm{TM}}+j\varphi_{\mathrm{TM},2}} + (\mathbf{z}\cdot\mathbf{E}_i)\mathbf{z}e^{-jk_0d\cos\theta_{\mathrm{TE}}+j\varphi_{\mathrm{TE},2}}]. \tag{2}$$

Note that the full transmission of both polarizations from the second metastructure is guaranteed due to reciprocity [32, 33]. Investigating (2), it is clear that the phase difference $\Delta\Phi = \Phi_{zz} - \Phi_{yy}$ for the transmitted wave is controllable with the distance "$d$", as well as choice of $\theta_{\mathrm{TM}}$ and $\theta_{\mathrm{TE}}$. For instance, if $\Delta\Phi$ is set at 90°, the metastructure in Figure 1 operates as a quarter waveplates, while for $\Delta\Phi$ of 180° we will have a half waveplate. This structure is analogous to a birefringent crystal, with the TE wave experiencing lower effective index (fast axis) and the TM wave is aligned with the slow axis with effective refractive index of 1 (assuming $\theta_{\mathrm{TE}}$ of 45° and $\theta_{\mathrm{TM}}$ of 0°). The waveplate is automatically "cut" in the right plate such that the fast and slow axes are parallel to the surface of the waveplate. In addition, note that we implicitly assume that if the metastructures are finite in the $y$-direction (i.e. a few periods of each surface are present), they are extended enough such that the waves will not spillover from the sides. As a rule of thumb, for Gaussian wave of waist $w_0$ focused on metastructure I, the structure must be extended at least to $y = (2w_0/\cos\theta)\sqrt{1+(\lambda_0 d/\pi w_0^2\cos\theta)^2} + d\tan\theta$, with $\theta = \max(\theta_{\mathrm{TM}}, \theta_{\mathrm{TE}})$.

Several techniques may be envisioned to attain polarization selective anomalous refraction. With electromagnetically thin surfaces, anomalous refraction can be created through carefully engineering the surface impedance profile to generate an effective constant momentum on the incident wave [34–36]. Along the same procedure, the surface profile maybe designed anisotropic (i.e. surface response depends on the polarization of the incident wave) to imprint a polarization dependent momentum on the wave [37, 38]. The choice of a specific technique to design such metastructures primarily depends on the wavelength of operation and the available computational resources. Here, we use optimization techniques (details in Sections 3 and 4) to create two sets of anisotropic metastructures complying with (2) and (4). While the performance of the system in Figure 1 is independent of the specifics of metastructures I and II (at the designed wavelength and angle of illumination), we note that several other properties of the system may strongly depend on the choice of platform. For instance, gradient metasurfaces have been shown to possess reasonably broadband behavior and angular stability [39, 40]. Such properties may not be automatically given using other platforms such as inverse design, yet, they can be encoded into the optimization [19, 22]. Here, we focused on narrowband optimization to demonstrate the

concept. However, available broadband optimization techniques may be used to create broadband devices.

Prior to characterizing the system and providing numerical examples, as a side note it is also worth mentioning the case of Panchantram-Berry (PB) or geometrical phase metastructures [41, 42]. Through systematic rotation of a half-waveplate surface element, PB metastructures create a desired phase profile on their surface which is used to alter the properties of the transmitted wave. For instance, by creating a linear phase profile (when each surface element is rotated by a constant degree compared to its neighboring elements), the momentum of the transmitted wave can be altered according to the slope of the phase profile. PB phase operates on circularly polarized (CP) incident fields and the imprinted phase flips sign depending on the handedness of the incident light [41]. As a result, left-and right-hand CP waves experience opposite transformations along interaction with PB metastructures. While in this article we focus on waveplates for orthogonal linearly polarized waves, it is also possible to use PB surfaces to achieve polarization conversion in a system similar to Figure 1, as explained briefly in the following: Assume metastructure I implemented using PB surface elements to change the direction of normally incident right-handed CP (RCP) plane waves by an angle of $\theta_{\mathrm{RCP}}$. Therefore, the left-handed incident wave (LCP) will be rotated by an angle of $\theta_{\mathrm{LCP}} = -\theta_{\mathrm{RCP}}$. Metastructure II is a 180° rotated version of metasurface I (see Figure 1 caption), thus it will restore the trajectory of each CP wave to normal direction. We note that due to $|\theta_{\mathrm{LCP}}| = |\theta_{\mathrm{RCP}}|$ for the normal incidence, both waves will experience equal retardation even though they are first split and then re-combined in the system. Let us now consider an obliquely incident "linearly polarized" wave (angle of incidence $\theta_{\mathrm{oblique}}$, defined as the angle between the wave vector and the vector normal to the metastructure I interface), illuminating the system from left to right. The linearly polarized wave can be expressed as the summation of two CP waves with opposite handedness, each experiencing their corresponding surface momentum. Following momentum conservation, the refraction angles in the area between metastructures I and II can be written as,

$$\theta'_{\mathrm{RCP}} = \sin^{-1}(\sin\theta_{\mathrm{RCP}} + \sin\theta_{\mathrm{oblique}}); \quad \theta'_{\mathrm{LCP}} = \sin^{-1}(\sin\theta_{\mathrm{LCP}} + \sin\theta_{\mathrm{oblique}}). \tag{3}$$

Consequently, by breaking the symmetry of refraction through oblique illumination we achieve $\theta'_{\mathrm{RCP}} \neq -\theta'_{\mathrm{LCP}}$ and RCP and LCP waves experience different propagation phases as they traverse the system. When re-combined at Metastructure II, the polarization state of the outgoing wave may be designed at will, for instance the system can be fully transformed the input into the orthogonal linear polarization (i.e. TE to TM conversion or vice versa). This is especially appealing considering the straightforward design procedure of PB metasurfaces. While in the following we focus on linear polarization (i.e. the surface momentum is designed for two orthogonal linearly polarized waves), the above discussion shows that similar argument is also valid for PB metasurfaces with proper considerations.

Returning to our design, following (2), the phase difference $\Delta\Phi = \Phi_{zz} - \Phi_{yy}$ can be written as,

$$\Delta\Phi = -k_0 d(\cos\theta_{\mathrm{TE}} - \cos\theta_{\mathrm{TM}}) + \varphi_{\mathrm{cte}} \tag{4}$$

in which $\varphi_{\mathrm{cte}}$ is a constant phase enclosing the local properties of metastructure I. For instance, assuming $\theta_{\mathrm{TE}}$ of 45° and $\theta_{\mathrm{TM}}$ of 0°, the system can be tuned from quarter waveplate functionality to half waveplate functionality through changing the separation of the metastructures by $\lambda_0/(4 - 2\sqrt{2})$. At 633 nm, this is about 540 nm tuning in the distance between metastructures. The tuning might be achieved through several effects to create mechanical movement such as using MEMS, motorized stages, flexible substrates, thermal expansion, electrostatic forces, etc. [43–49]. For instance, MEMS tunable metasurface devices have been shown to offer micron-scale distance tunability [45], enough to achieve arbitrary retardation control in our example.

### 2.2. *Oblique incidence*

Equation (4) is written for the case of normal illumination on the system. Interestingly, the design in Figure 1 may also provide a platform for dual (or multiple) functionality under oblique incidence. Let us consider an incident angle of $\theta_{\text{inc}}$ (angle between the wave vector and the vector normal to the metastructure I interface, in the plane of incidence). Assuming $\theta_{\text{inc}}$ to be small enough such that the structure is still reflectionless, the imprinted momentum enforces the refracted angles of the TM and TE waves to be (in the region between metastructures I and II),

$$\theta'_{\text{TE}} = \sin^{-1}(\sin\theta_{\text{TE}} + \sin\theta_{\text{inc}}), \quad \theta'_{\text{TM}} = \sin^{-1}(\sin\theta_{\text{TM}} + \sin\theta_{\text{inc}}). \tag{5}$$

As a result, the phase shift between the orthogonal polarizations is a function of incidence angle following,

$$\Delta\Phi' = -k_0 d(\cos\theta'_{\text{TE}} - \cos\theta'_{\text{TM}}) + \varphi'_{\text{cte}}. \tag{6}$$

There are several possibilities to use such form of dependence on the illumination angle. For example, one can imagine a structure specifically tuned to create half waveplate response for normal incidence and quarter waveplate response for oblique incidence. As another example, one can imagine a system correcting unwanted phase shifts depending on the angle of incidence. Clearly, exploiting the angular response of the system requires metastructures to be designed with reasonable angular stability. As mentioned, gradient metasurfaces typically maintain their performance over a wide range of incident angles [39, 40]. If other platforms are used, this property is to be built in the optimization procedure [19, 22].

## 3. Numerical results: Part I

In this section we present a set of numerical results to elucidate the principles of the operation of the proposed system, implementing a tunable waveplate. While the principles of the operation are similar, the same functionality may be implemented in several platforms and with distinct characteristics that maybe required for a specific application. Fabrication limitations, desired operational bandwidth and dispersion characteristics, availability of materials, desired angular response, and insertion loss are some of the main parameters that affect the choice of platform. Here, we start by an inverse-designed topology-optimized dielectric structures exploiting the entire design space (Section 3) and continue with topology-optimized complex multilayer structures with the goal of better compatibility with currently available fabrication techniques.

Figure 2 shows a set of four optimized geometries to achieve waveplate operation, following the schematic demonstration in Figure 1 (four separate examples are provided). The distribution of the permittivity inside each of the four metastructures is optimized such that the structure imprints zero momentum shift on the incident TM wave ($\theta_{\text{TM}}$ is 0°) and constant momentum shift on the incident TE waves ($\theta_{\text{TE}}$ is 45°). We exploit low-loss materials (e.g. $TiO_2$ with permittivity of approximately 5.5 at 633 nm [50]) as shown in panel (a), as well as higher index materials (e.g. Silicon with approximate permittivity of 11.7 at 3000 nm [51]), as shown in panel (b). In each case, topology optimization [52] is used to find the distribution of permittivity, enforcing a quantized pattern as much as possible. In this regard, we are looking for patterns consisting of either air (blue) or dielectric (pink). This is especially clear in Figure 2b where we could achieve a bi-material pattern (Silicon and air) due to high refractive index of Silicon. We also note that the availability of materials play a crucial role on the size of the metastructures. In our examples shown in Figure 2, desired functionality was achieved over a thickness of approximately $0.8\lambda_0$ at 633 nm and $0.25\lambda_0$ at 3000 nm. Clearly, adding additional constraints on the optimization (such as angular stability, broadband operation, less granularity, etc. as discussed above) will entail larger structures. In the following, we will present the simulation results for the structure

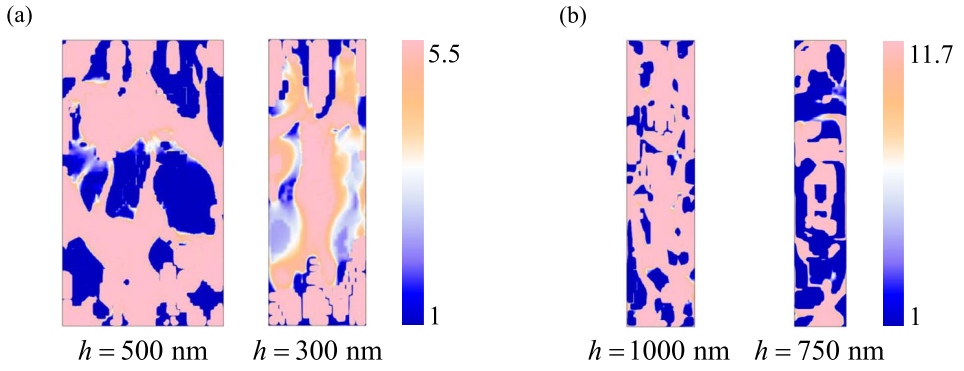


**Figure 2.** Inverse-design topology-optimized permittivity distributions to achieve polarization-dependent momentum control. The distribution of relative permittivity inside metastructure I in Figure 1 for $\theta_{TE}$ of 45° and $\theta_{TM}$ of 0°, optimized for two different thickness at (a) 633 nm when colors indicate $TiO_2$ and air at the extreme values, and (b) 3000 nm when colors indicate Si and $SiO_2$ at the extreme values. In each case, one unit cell in the $y$-direction is shown. The second case in panel (a) exhibits graded permittivity distribution, while the three other examples are approximately quantized.

shown in Figure 2a-left panel. The other three examples offer similar performances. The overall response of the system as shown in Figure 1, is indeed predominantly set based on the accuracy in the design of metastructure I. As a result, as long as efficient polarization-dependent beam splitting is achieved with metastructure I, the entire system operates efficiently following (4).

Enforcing $\theta_{TE}$ to be 45° (and $\theta_{TM}$ being 0°) requires a periodicity of $1.4\lambda_0$ for the structure in the $y$-direction [40]. This is approximately 900 nm at the design wavelength of 633 nm in the visible range. Optimization goals are set as simultaneous total transmission into zeroth order mode for the TM polarization and total transmission to the first order Floquet mode ($n = 1$) for the TE polarization. We note that the choice of $\theta_{TE}$ is arbitrary, and as it can be seen in Section 3.1, it merely affects the sensitivity of the waveplate operation to variations in the distance between the two metastructures. On the other hand, extreme angles of propagation in the area between metastructure I and II may be more difficult to achieve while maintaining full transparency. Figure 3 demonstrates the performance of the optimized structure shown in Figure 2a-left panel. Simulations are performed in COMSOL Multiphysics® using the frequency domain solver [52]. The optimized topology is capable of transforming more than 99% of the incident power into the desired diffraction modes for both polarization states of the incident wave. While the distribution of the wave inside the optimized layer exhibits complicated behavior, the evanescent decay is quite rapid and after a distance of approximately half a wavelength the desired scattering mode is dominant. This implies that when assembling the system in Figure 1, we can bring the surfaces as close as 300 nm for operation at 633 nm wavelength. Inspecting the field distributions in Figure 3, we note that the y-component of the electric field shown in the lower panel is not the tangential component of the field in the dielectric region. As a result, this component is mostly discontinuous across the dielectric region. This does not imply higher Q modes in the case of TM illumination. Indeed, one might look at the distribution of the $z$-component of the magnetic field in this case, which is continuous across all layers.

In the next step, two metastructures with the profile shown in Figure 2a-left panel are arranged cascaded (see Figure 1) with proper rotation of the second metastructure to achieve controllable retardation. The results are qualitatively portrayed in Figure 4 where we show time snapshot of the electric field distribution when the cascaded system is illuminated with TE and TM fields,

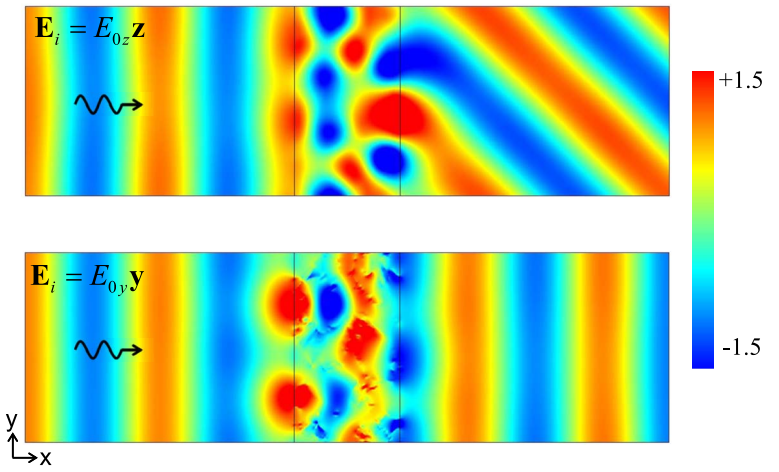


**Figure 3.** Polarization beam splitting metastructure. Snapshot in time of numerical simulation of electric field distribution when metastructure shown in Figure 2a-left panel is illuminated from left side with a plane wave (normal to the structure interface, i.e. $\theta_{\text{inc}} = 0$). The upper panel shows the distribution of the $z$-component of the electric field for TE illumination (i.e. $\mathbf{E}_i = E_{0z}\mathbf{z}$). The entire incident energy is funneled into the first order transmission Floquet mode, designed at $\theta_{\text{TE}}$ equal to 45°. The topology-optimized metastructure creates a complex near-field in the vicinity of the structure, however the evanescent waves decay rapidly. The lower panel shows the distribution of the y-component of the electric field for TM illumination (i.e. $\mathbf{E}_i = E_{0y}\mathbf{y}$). The entire incident energy is funneled into the zeroth-order transmission Floquet mode, indicating $\theta_{\text{TM}}$ equal to 0°. Note that in this case, the plotted component of the electric field (i.e. $y$-component) is not tangent to the metastructure pattern boundaries. As the result, the field distribution is discontinuous at the air-dielectric interfaces. Here, we have used COMSOL Multiphysics® frequency domain solver [52]. The structure is truncated with periodic boundaries at the top and bottom, linked to two periodic ports on the left (for excitation) and right. The polarization of the incident field is set at the ports and all incident waves are normal to the surface of the optimized structure, i.e. propagating in the $x$-direction.

respectively shown in the upper and lower panels. As expected, the wave experiences a different trajectory in the area between the two metastructures depending on the polarization of the incident wave. As viewed from the outside, normally incident waves experience polarization-dependent retardation as they traverse the system. Here we show four examples with the phase delay between the two polarizations changing between 0° (Figure 4a), 90° (Figure 4b), 180° (Figure 4c), and 270° (Figure 4d). Clearly, any other value of phase retardation can be achieved by adjusting the distance between the two layers in the values between such distances. Each degree of change in retardation requires a movement of approximately 6 nm in the distance between metastructures (see (4)).

The results are quantitatively studied in Figure 5 where we show the transmission amplitudes and phases as a function of the separation "d". As expected, the transmission amplitudes (Figure 5a) are very high for both polarizations and above 95% power transmission for TE wave and above 99% power transmission for the TM wave are achieved, independent of the spacing between metastructures. This is the direct result of enforcing zero reflection in the topology-optimized design of metastructure I, which ensures minimal Fabry–Pérot effects. The amplitude

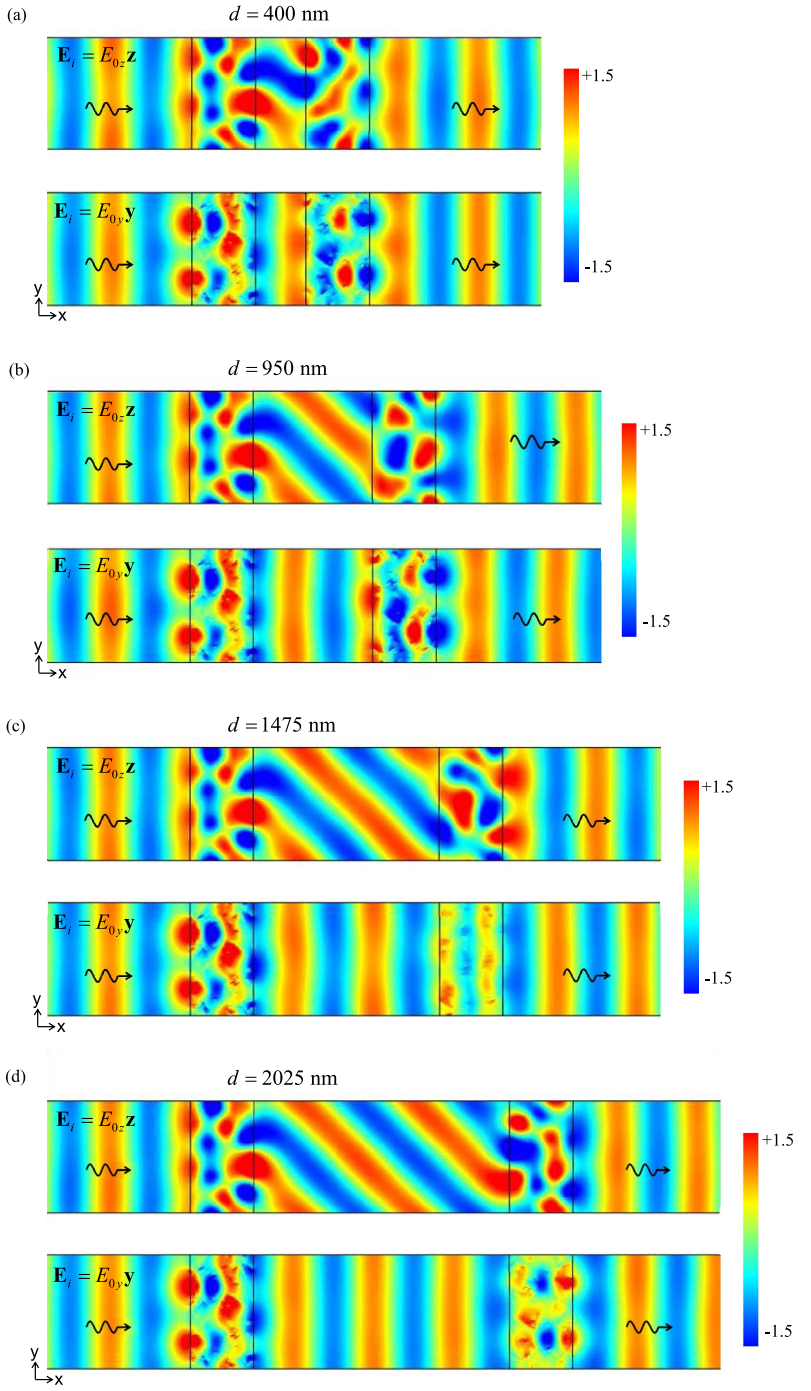


**Figure 4.** Tunable retardation. Snapshot in time of the numerical simulation of electric field distribution (both polarizations) for different values of "d" parameter, as shown in Figure 1. Metastructures I and II are identical and 180° rotated version of each other. Due to proper cascading, TE and TM waves experience different trajectories in the area between the two metastructures, but they merge after the second metastructure. The axial separation between metastructures (i.e. "d") is chosen such that the phase shift between two polarizations is (a) 0°, (b) 90°, (c) 180°, and (b) 270°. Details on the simulation setup are given in the caption of Figure 3.

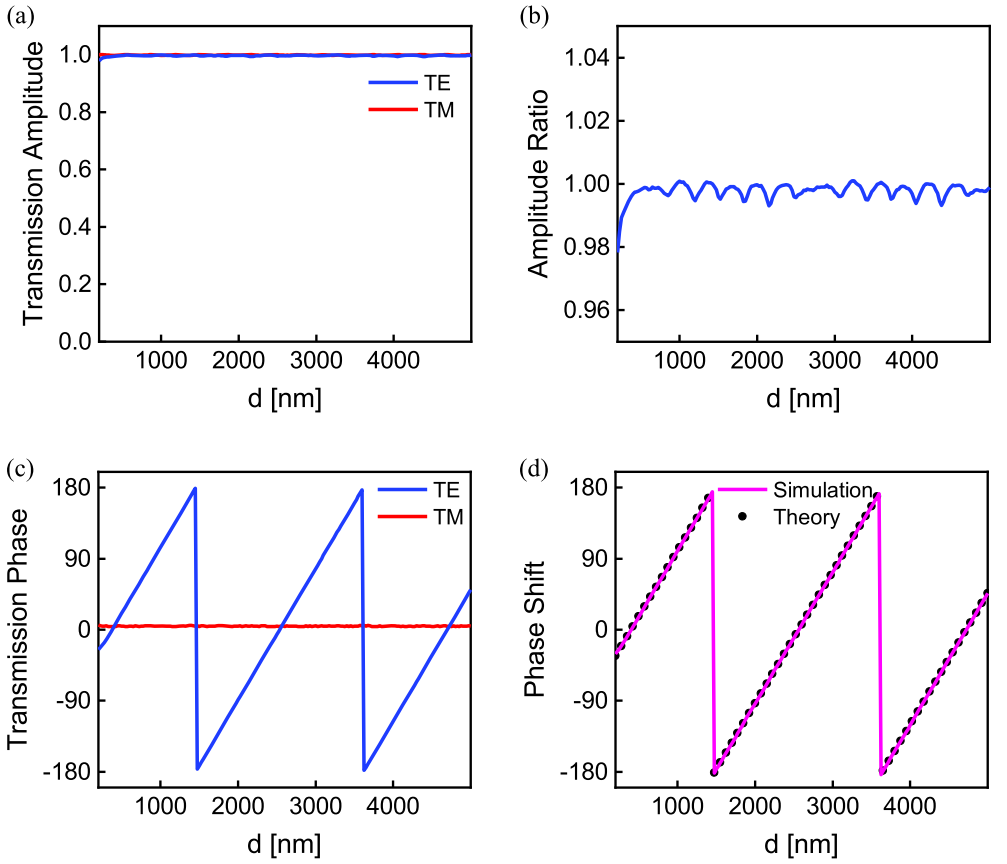


**Figure 5.** Tunable waveplate characterization. Simulation results for (a) Transmission amplitude of the TE (blue) and TM (red) normally incident plane waves from the waveplate system (shown in Figures 1 and 2a-left panel). Due to enforcing zero reflection in the optimization procedure, no resonance effect is observed. (b) Amplitude ratio defined as the ratio between the transmission amplitude of the TE wave divided by the transmission amplitude of the TM wave. (c) Transmission phase of the TE (blue) and TM (red) normally incident plane waves. Phases are recorded at constant positions regardless of the distance "d". Since the TM refraction angle is chosen at 0°, i.e. $\theta_{TM} = 0$, the output phase is not a function of "d" for this polarization. (d) Phase difference between the outgoing waves, compared to the analytical expression given in (4).

ratio between the transmitted TE and TM waves is also shown in Figure 5b, maintaining approximate ratio of 1 across all values of "d". The transmission phase of the two polarization components versus the spacing "d" is shown in Figure 5c. Note that the inner refraction angles are set at $\theta_{TM} = 0°$ and $\theta_{TE} = 45°$. As a result, the outgoing phase of the TM wave is not a function of "d", merely maintaining a constant value due to the local constant phases added by metastructures. The transmission phase of the TE wave, on the other hand, follows a slope of $-k_0(\cos\theta_{TE} - 1)$, as the sampling ports are positioned at fixed distances from each other. Figure 5d illustrated the simulated phase difference $\Delta\Phi = \Phi_{TE} - \Phi_{TM}$ compared with the expected linear variation calculated in (4), showing very good agreement.

### 3.1. *Extreme bending*

Figure 5d (along with the approximately constant amplitude ratio reported in Figure 5b) illustrates the tunable waveplate operation of the system. As mentioned before for our choice of refraction angles an axial distance variation of approximately 540 nm is required to change the retardation by 90° (6 nm change for each degree of retardation). More rigorously, this length can be expressed as a function of both refraction angles as,

$$\Delta d_{\pi/2} = \frac{\lambda_0}{4|\cos\theta_{\mathrm{TE}} - \cos\theta_{\mathrm{TM}}|}. \tag{7}$$

Evidently, by maximizing the denominator in (7) we can increase the sensitivity of the waveplate. As an example of this high sensitivity, we have used topology optimization to design metastructures with $\theta_{\mathrm{TM}}$ of 0° and extreme $\theta_{\mathrm{TE}}$ of 85°. Clearly, the extreme wave bending would entail a more sophisticated optimization procedure [36]. Here, we adhere to the same size and materials as used for the previous example to provide a sample design. The optimized metastructure couples approximately 98% of the incident TE wave power to the first Floquet mode and more than 99% of the incident TM wave to the zeroth order transmission mode. Figure 6a visually illustrates the performance of the waveplate when adjusted to create 180° phase shift between TE and TM waves (half-wave plate operation). Note the extreme bending in the area between the two metastructures under TE illumination. It is worth mentioning that power conservation requires that amplitude of the refracted wave to be inversely related to the incident normal wave [36]. For this reason, the wave in the area between the two metastructures shows a higher amplitude although it carries the same amount of power as the incident wave. There are no internal reflections or resonance behaviors involved and the wave smoothly propagates from left to right.

Due to high angle of refraction for the TE wave, cascading the two surfaces is quite challenging due to the possibility of internal reflections. This is quantified in Figure 6b, where the transmission amplitude of both polarizations is studied for different values of separation. Indeed, and in spite of the internal extreme bending, we are able to achieve a range with width of approximately 2000 nm where transmission amplitudes are approximately constant. The internal reflections create resonances beyond these points, which are to be avoided. In this range, as shown in Figure 6c, the phase shift between the two linear polarizations approximately follow the expected trajectory in (4). We note that the optimal phase trajectory is calculated for a reflectionless structure. As a result, when there is residual reflection from metastructures, or internal resonances are created, the phase shift differs from the optimal value reported in (4). Here, to switch from quarter-wave plate operation to half-wave plate operation at wavelength of 633 nm (i.e. 90° retardation change), the separation must be changed approximately 170 nm (less than 2 nm change for each degree of retardation). As discussed before, depending on the application, the sensitivity of the waveplate may be controlled through proper choice of $\theta_{\mathrm{TE}}$ and $\theta_{\mathrm{TM}}$.

## 4. Numerical results: Part II

The results presented in Section 3 utilized the entire design space to provide topology-optimized metastructures for tunable waveplate operation. In this section we report another example designed using the genetic algorithm optimization technique and enforcing a multi-layer structure (similar to [22]), suitable for possible fabrication. Structure is designed at mid-infrared (3000 nm) in form of silicon posts embedded in alumina (shown in Figure 7a). Silicon posts are approximately 230 nm tall in $x$-direction and the minimum width of each post is more than 200 nm in $y$-direction. Genetic algorithm minimization [53] is used to define the optimum material in each pixel (total of 107 degrees of freedom). We assume $\theta_{\mathrm{TM}}$ to be 0° and $\theta_{\mathrm{TE}}$ of 45°. The corresponding transmission amplitudes and phase retardation between the two polarizations are shown in

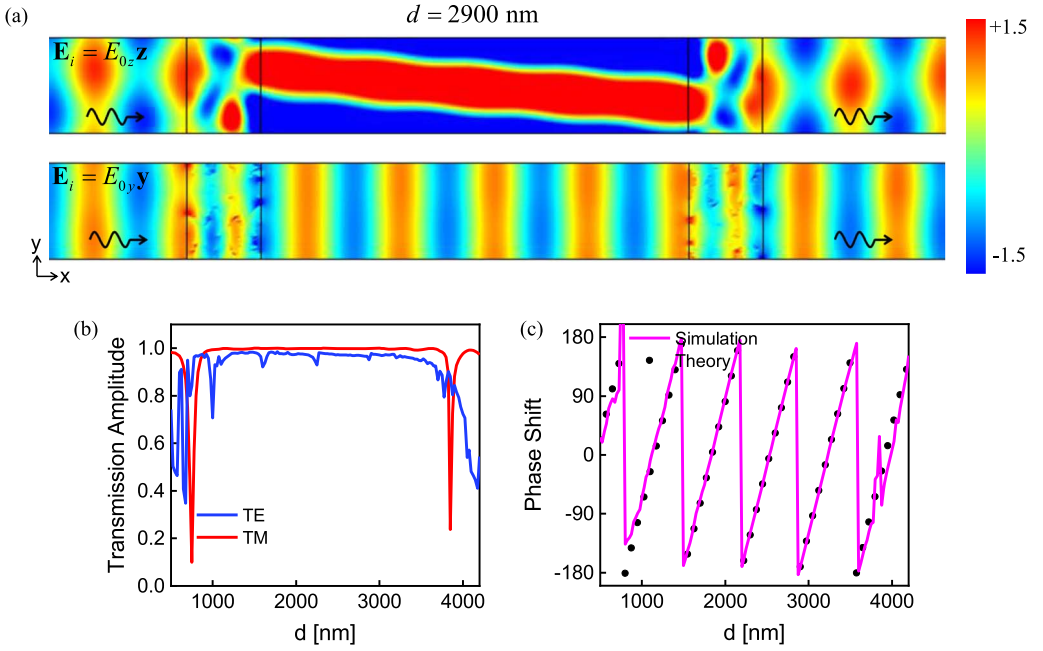


**Figure 6.** Tunable retardation with increased sensitivity. (a) Snapshot in time of numerical simulation of electric field distribution (both polarizations) for "d" parameter set at 2900 nm to provide a phase shift of 180° between two polarizations. Due to proper cascading, TE and TM waves experience different trajectories in the area between the two metastructures, but they merge after the second metastructure. (b) Transmission amplitude of the TE (blue) and TM (red) normally incident plane waves from the waveplate system when the internal angles are set to 85° for TE wave and 0° for the TM wave. (c) Phase difference between the outgoing waves, compared to the analytical expression given in (4), plotted versus separation "d". Details on the simulation setup are given in the caption of Figure 3. Here, due to the extreme bending angle and the enhanced sensitivity of response to the granularity of the metastructure, identical mesh profiles are used at the optimization and simulation stages. The response sensitivity may be controlled as a parameter in the optimization process.

Figures 7b and 7c, respectively. Here, there are residual unwanted scattering in metastructure I (which may be eliminated with further genetic algorithm optimization) around 14% for TE and 10% for TM waves. As a result, there is a fluctuation in the amplitude of the desired outgoing wave. The phase profile, however, is more resilient to such scatterings, as can be seen in Figure 7c.

## 5. Conclusions

We have numerically presented a new approach to achieve tunable waveplate operation using two cascaded metastructures. Metastructures are identical and designed to operate as polarization-sensitive beam splitters with designer refraction angles. It is shown that with proper arrangements, the phase delay between the two linearly polarized illuminating waves can be tuned by changing the distance between the metastructures. This can be envisioned through using MEMS, motorized stages, flexible substrates, or thermal expansion. The full retardation control (and hence control on the ellipticity of the outgoing wave) is attainable through wavelength-

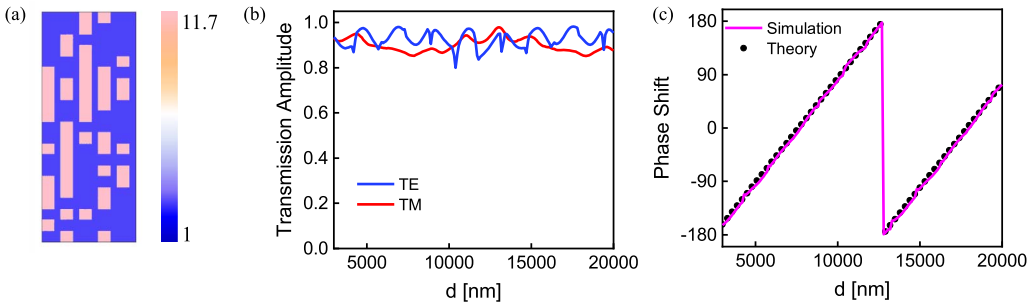


**Figure 7.** Multi-layer tunable waveplate. (a) Distribution of relative permittivity inside metastructure I. The pink color corresponds to silicon posts and the light blue background shows the alumina substrate. (b) Transmission amplitude of the TE (blue) and TM (red) normally incident plane waves from the waveplate system shown in panel a. (c) Phase difference between orthogonal polarizations of the outgoing wave, compared with the analytical expression given in (4), plotted versus separation "d".

scale axial distance variations. The internal refraction angles maybe used to control the sensitivity of the waveplate. Dual or multiple functionality is also possible by changing the incident angle. Implications of using geometrical phase (PB phase) to achieve linear polarization conversion is also discussed. Topology-optimized physical designs of waveplates for operation at visible and mid-infrared are presented. We consider both cases of full design space and restricted multi-layer optimizations using the commercial numerical solvers. In addition to tunable waveplate operation at typical cases of quarter and half-waveplate, the proposed structure is especially interesting to restore the desired polarization when unwanted phase shifts are created between orthogonal polarization components, in complex multi-elements setups. One of the key characteristics of the presented approach relies on the decoupling between the induced phase shift and the individual properties of the metastructure. We showed that the phase shift can be controlled with variation of a single physical parameter. This significantly reduces the complexity of the design procedure. With the growing interest in using metasurfaces in new realms (e.g. for non-electromagnetic waves [54–56] or non-classical waves [57–60]), our approach may find interesting applications in the broader metamaterial community.

## Acknowledgements

This work is supported in part by the US Air Force Office of Scientific Research (AFOSR) Multidisciplinary University Research Initiative (MURI) grant # FA9550-17-1-0002.

## References

[1] G. Ghosh, "Dispersion-equation coefficients for the refractive index and birefringence of calcite and quartz crystals", *Opt. Commun.* **163** (1999), no. 1–3, p. 95-102.
[2] N. Yu, F. Aieta, P. Genevet, M. A. Kats, Z. Gaburro, F. Capasso, "A broadband, background-free quarter-wave plate based on plasmonic metasurfaces", *Nano Lett.* **12** (2012), no. 12, p. 6328-6333.
[3] B. Yang, W. Ye, X. Yuan, Z. Zhu, C. Zeng, "Design of ultrathin plasmonic quarter-wave plate based on period coupling", *Opt. Lett.* **38** (2013), no. 5, p. 679-681.
[4] L. Cong, N. Xu, J. Gu, R. Singh, J. Han, W. Zhang, "Highly flexible broadband terahertz metamaterial quarter-wave plate", *Laser Photonics Rev.* **8** (2014), no. 4, p. 626-632.
[5] A. Roberts, L. Lin, "Plasmonic quarter-wave plate", *Opt. Lett.* **37** (2012), no. 11, p. 1820-1822.

[6] M. Mutlu, A. E. Akosman, G. Kurt, M. Gokkavas, E. Ozbay, "Experimental realization of a high-contrast grating based broadband quarter-wave plate", *Opt. Express* **20** (2012), no. 25, p. 27966-27973.
[7] A. Pors, S. I. Bozhevolnyi, "Efficient and broadband quarter-wave plates by gap-plasmon resonators", *Opt. Express* **21** (2013), no. 3, p. 2942-2952.
[8] Y. Zhao, A. Alu, "Tailoring the dispersion of plasmonic nanorods to realize broadband optical meta-waveplates", *Nano Lett.* **13** (2013), no. 3, p. 1086-1091.
[9] A. Pors, M. G. Nielsen, S. I. Bozhevolnyi, "Broadband plasmonic half-wave plates in reflection", *Opt. Lett.* **38** (2013), no. 4, p. 513-515.
[10] S. Jiang, X. Xiong, Y. Hu, Y. Hu, G. Ma, R. Peng, C. Sun, M. Wang, "Controlling the polarization state of light with a dispersion-free metastructure", *Phys. Rev. X* **4** (2014), no. 2, article no. 021026.
[11] Z. H. Jiang, L. Lin, D. Ma, S. Yun, D. H. Werner, Z. Liu, T. S. Mayer, "Broadband and wide field-of-view plasmonic metasurface-enabled waveplates", *Sci. Rep.* **4** (2014), p. 7511.
[12] F. Ding, Z. Wang, S. He, V. M. Shalaev, A. V. Kildishev, "Broadband high-efficiency half-wave plate: a supercell-based plasmonic metasurface approach", *ACS Nano* **9** (2015), no. 4, p. 4111-4119.
[13] D. Wang, Y. Gu, Y. Gong, C. Qiu, M. Hong, "An ultrathin terahertz quarter-wave plate using planar babinet-inverted metasurface", *Opt. Express* **23** (2015), no. 9, p. 11114-11122.
[14] P. I. Borel, A. Harpøth, L. H. Frandsen, M. Kristensen, P. Shi, J. S. Jensen, O. Sigmund, "Topology optimization and fabrication of photonic crystal structures", *Opt. Express* **12** (2004), no. 9, p. 1996-2001.
[15] J. S. Jensen, O. Sigmund, "Topology optimization for nano-photonics", *Laser Photonics Rev.* **5** (2011), no. 2, p. 308-321.
[16] C. M. Lalau-Keraly, S. Bhargava, O. D. Miller, E. Yablonovitch, "Adjoint shape optimization applied to electromagnetic design", *Opt. Express* **21** (2013), no. 18, p. 21693-21701.
[17] B. Shen, P. Wang, R. Polson, R. Menon, "An integrated-nanophotonics polarization beamsplitter with 2. 4 × 2. 4 $\mu m^2$ footprint", *Nat. Photonics* **9** (2015), no. 6, p. 378.
[18] Y. Noguchi, T. Yamada, M. Otomori, K. Izui, S. Nishiwaki, "An acoustic metasurface design for wave motion conversion of longitudinal waves to transverse waves using topology optimization", *Appl. Phys. Lett.* **107** (2015), no. 22, article no. 221909.
[19] A. Y. Piggott, J. Lu, K. G. Lagoudakis, J. Petykiewicz, T. M. Babinec, J. Vuckovic, "Inverse design and demonstration of a compact and broadband on-chip wavelength demultiplexer", *Nat. Photonics* **9** (2015), no. 6, p. 374.
[20] F. Callewaert, V. Velev, P. Kumar, A. V. Sahakian, K. Aydin, "Inverse-designed broadband all-dielectric electromagnetic metadevices", *Sci. Rep.* **8** (2018), no. 1, p. 1358.
[21] Z. Lin, L. Christakis, Y. Li, E. Mazur, A. W. Rodriguez, M. Lončar, "Topology-optimized dual-polarization Dirac cones", *Phys. Rev. B* **97** (2018), no. 8, article no. 081408.
[22] Z. Lin, B. Groever, F. Capasso, A. W. Rodriguez, M. Loncar, "Topology-optimized multilayered metaoptics", *Phys. Rev. Appl.* **9** (2018), no. 4, article no. 044030.
[23] N. Mohammadi Estakhri, B. Edwards, N. Engheta, "Inverse-designed metastructures that solve equations", *Science* **363** (2019), no. 6433, p. 1333-1338.
[24] R. C. Sharp, D. P. Resler, D. S. Hobbs, T. A. Dorschner, "Electrically tunable liquid-crystal wave plate in the infrared", *Opt. Lett.* **15** (1990), no. 1, p. 87-89.
[25] L. Wang, X. W. Lin, W. Hu, G. H. Shao, P. Chen, L. J. Liang, B. B. Jin, P. H. Wu, H. Qian, Y. N. Lu, X. Liang, "Broadband tunable liquid crystal terahertz waveplates driven with porous graphene electrodes", *Light Sci. Appl.* **4** (2015), no. 2, article no. e253.
[26] L. Wang, S. Ge, W. Hu, M. Nakajima, Y. Lu, "Tunable reflective liquid crystal terahertz waveplates", *Opt. Mater. Express* **7** (2017), no. 6, p. 2023-2029.
[27] D. Wang, L. Zhang, Y. Gu, M. Q. Mehmood, Y. Gong, A. Srivastava, L. Jian, T. Venkatesan, C. Qiu, M. Hong, "Switchable ultrathin quarter-wave plate in terahertz using active phase-change metasurface", *Sci. Rep.* **5** (2015), p. 15020.
[28] T. Li, L. Huang, J. Liu, Y. Wang, T. Zentgraf, "Tunable wave plate based on active plasmonic metasurfaces", *Opt. Express* **25** (2017), no. 4, p. 4216-4226.
[29] X. Zhao, J. Schalch, J. Zhang, H. R. Seren, G. Duan, R. D. Averitt, X. Zhang, "Electromechanically tunable metasurface transmission waveplate at terahertz frequencies", *Optica* **5** (2018), no. 3, p. 303-310.
[30] B. E. Saleh, M. C. Teich, *Fundamentals of Photonics*, 3rd ed., John Wiley & Sons, 2019.
[31] N. Mohammadi Estakhri, N. Engheta, "Free-space optical Mach-Zehnder modulator based on two cascaded metasurfaces", in *CLEO: Applications and Technology*, Optical Society of America, 2018, p. JW2A-93.
[32] V. H. Rumsey, "Reaction concept in electromagnetic theory", *Phys. Rev.* **94** (1954), no. 6, p. 1483.
[33] G. Whitman, F. Schwering, "Reciprocity identity for periodic surface scattering", *IEEE Trans. Antennas Propag.* **27** (1979), no. 2, p. 252-254.
[34] N. Yu, P. Genevet, M. A. Kats, F. Aieta, J. Tetienne, F. Capasso, Z. Gaburro, "Light propagation with phase discontinuities: generalized laws of reflection and refraction", *Science* **334** (2011), no. 6054, p. 333-337.
[35] C. Pfeiffer, A. Grbic, "Metamaterial Huygens' surfaces: tailoring wave fronts with reflectionless sheets", *Phys. Rev. Lett.* **110** (2013), no. 19, article no. 197401.

[36] N. Mohammadi Estakhri, A. Alu, "Wave-front transformation with gradient metasurfaces", *Phys. Rev. X* **6** (2016), no. 4, article no. 041008.
[37] S. Kruk, B. Hopkins, I. Kravchenko, A. Miroshnichenko, D. N. Neshev, Y. S. Kivshar, "Invited article: broadband highly efficient dielectric metadevices for polarization control", *APL Photonics* **1** (2016), no. 3, article no. 030801.
[38] J. P. B. Mueller, N. A. Rubin, R. C. Devlin, B. Groever, F. Capasso, "Metasurface polarization optics: independent phase control of arbitrary orthogonal states of polarization", *Phys. Rev. Lett.* **118** (2017), no. 11, article no. 113901.
[39] S. Sun, K. Yang, C. Wang, T. Juan, W. T. Chen, C. Y. Liao, Q. He, S. Xiao, W. T. Kung, G. Y. Guo, L. Zhou, "High-efficiency broadband anomalous reflection by gradient meta-surfaces", *Nano Lett.* **12** (2012), no. 12, p. 6223-6229.
[40] N. Mohammadi Estakhri, A. Alu, "Manipulating optical reflections using engineered nanoscale metasurfaces", *Phys. Rev. B* **89** (2014), no. 23, article no. 235419.
[41] E. Hasman, V. Kleiner, G. Biener, A. Niv, "Polarization dependent focusing lens by use of quantized Pancharatnam–Berry phase diffractive optics", *Appl. Phys. Lett.* **82** (2003), no. 3, p. 328-330.
[42] X. Chen, L. Huang, H. Muhlenbernd, G. Li, B. Bai, Q. Tan, G. Jin, C. Qiu, S. Zhang, T. Zentgraf, "Dual-polarity plasmonic metalens for visible light", *Nat. Commun.* **3** (2012), p. 1198.
[43] Y. Zou, W. Zhang, F. S. Chau, G. Zhou, "Miniature adjustable-focus endoscope with a solid electrically tunable lens", *Opt. Express* **23** (2015), no. 16, p. 20582-20592.
[44] M. Baranski, S. Bargiel, N. Passilly, C. Gorecki, C. Jia, J. Fromel, M. Wiemer, "Micro-optical design of a three-dimensional microlens scanner for vertically integrated micro-opto-electro-mechanical systems", *Appl. Opt.* **54** (2015), no. 22, p. 6924-6934.
[45] E. Arbabi, A. Arbabi, S. Kamali, Y. Horie, M. Faraji-Dana, A. Faraon, "MEMS-tunable dielectric metasurface lens", *Nat. Commun.* **9** (2018), no. 1, p. 812.
[46] A. Zhan, S. Colburn, C. M. Dodson, A. Majumdar, "Metasurface freeform nanophotonics", *Sci. Rep.* **7** (2017), no. 1, p. 1673.
[47] H.-S. Ee, R. Agarwal, "Tunable metasurface and flat optical zoom lens on a stretchable substrate", *Nano Lett.* **16** (2016), no. 4, p. 2818-2823.
[48] S. Lee, H. Tung, W. Chen, W. Fang, "Thermal actuated solid tunable lens", *IEEE Photonics Technol. Lett.* **18** (2006), no. 21, p. 2191-2193.
[49] J. Ou, E. Plum, J. Zhang, N. I. Zheludev, "An electromechanically reconfigurable plasmonic metamaterial operating in the near-infrared", *Nat. Nanotechnol.* **8** (2013), no. 4, p. 252.
[50] R. C. Devlin, M. Khorasaninejad, W. T. Chen, J. Oh, F. Capasso, "Broadband high-efficiency dielectric metasurfaces for the visible spectrum", *Proc. Natl Acad. Sci. USA* **113** (2016), no. 38, p. 10473-10478.
[51] H. W. Icenogle, B. C. Platt, W. L. Wolfe, "Refractive indexes and temperature coefficients of germanium and silicon", *Appl. Opt.* **15** (1976), no. 10, p. 2348-2351.
[52] Comsol, Topology optimizations are performed with COMSOL optimization module, using SNOPT method. Forward simulations are performed using RF module in the frequency domain. www.comsol.com.
[53] Comsol, Genetic algorithm minimizations are performed in MATLAB (https://www.mathworks.com/) using LiveLink interface (https://www.comsol.com/livelink-for-matlab).
[54] Y. Jin, R. Kumar, O. Poncelet, O. Mondain-Monval, T. Brunet, "Flat acoustics with soft gradient-index metasurfaces", *Nat. Commun.* **10** (2019), no. 1, p. 1-6.
[55] Z. Tian, C. Shen, J. Li, E. Reit, Y. Gu, H. Fu, S. A. Cummer, T. J. Huang, "Programmable acoustic metasurfaces", *Adv. Funct. Mater.* **29** (2019), no. 13, article no. 1808489.
[56] S. Inampudi, J. Cheng, M. M. Salary, H. Mosallaei, "Unidirectional thermal radiation from a SiC metasurface", *J. Opt. Soc. Amer. B* **35** (2018), no. 1, p. 39-46.
[57] S. I. Bozhevolnyi, "Shaping wavefronts of single photons with metasurfaces (Conference Presentation)", in *Proc. SPIE 11344, Metamaterials XII, 113440O (1 April 2020)*, SPIE, 2020.
[58] N. M. Estakhri, T. B. Norris, "Controlling quantum interference using metamaterials", in *Proc. SPIE 11091, Quantum Nanophotonic Materials, Devices, and Systems 2019, 110911D (3 September 2019)*, SPIE, 2019.
[59] P. Georgi, M. Massaro, K.-H. Luo, B. Sain, N. Montaut, H. Herrmann, T. Weiss, G. Li, C. Silberhorn, T. Zentgraf, "Metasurface interferometry toward quantum sensors", *Light: Sci. Appl.* **8** (2019), no. 1, p. 1-7.
[60] R. Bekenstein, I. Pikovski, H. Pichler, E. Shahmoon, S. F. Yelin, M. D. Lukin, "Quantum metasurfaces with atom arrays", *Nat. Phys.* (2020), p. 1-6.